# Out-of-plane compression of a novel hybrid corrugated core sandwich panel

Shanyouming Sun [a,c,d], Dan Liu [b], Yinglong Sheng [a], Shangsheng Feng [d,e,*], Hongbin Zhu [f], Tian Jian Lu [c,g,*]

[a] State Key Laboratory for Strength and Vibration of Mechanical Structures, Xi'an Jiaotong University, Xi'an 710049, PR China
[b] Xi'an Aerospace Yuan Dongli Engineering Co., Ltd., Xi'an 710100, PR China
[c] State Key Laboratory of Mechanics and Control of Mechanical Structures, Nanjing University of Aeronautics and Astronautics, Nanjing 210016, PR China
[d] Bioinspired Engineering and Biomechanics Center (BEBC), Xi'an Jiaotong University, Xi'an 710049, PR China
[e] The Key Laboratory of Biomedical Information Engineering of Ministry of Education, School of Life Science and Technology, Xi'an Jiaotong University, Xi'an 710049, PR China
[f] CRRC Industrial Academy Co., Ltd., China Railway Rolling Stock Corporation (CRRC), Beijing, 100161, PR China
[g] MIIT Key Laboratory of Multifunctional Lightweight Materials and Structures (MLMS), Nanjing University of Aeronautics and Astronautics, Nanjing 210016, PR China

## ARTICLE INFO

## ABSTRACT

Lightweight sandwich panels with fluid-through cellular cores are promising for applications requiring simultaneous load-bearing and heat dissipation such as the combustion chamber of scramjet. While existing core topologies have exhibited good designability for specific thermal or mechanical requirements, the increasing demand for multifunctional attributes usually points to different core topology designs. Finding a single core topology that possesses excellent mechanical and thermal properties simultaneously remains challenging. To address the issue, the concept of a hybrid core (termed herein as the N core) that combines the conventional corrugated core with the web core was proposed to mitigate confliction between thermal and mechanical designs. Out-of-plane compressive characteristics of the hybrid cored sandwich panel was investigated theoretically, numerically and experimentally. An elastic–plastic analytical model was developed to predict the out-of-plane compressive behavior, with connection strength between facesheets and core as well as non-uniform strut thickness accounted for. For validation, test sample was fabricated using 3D-printing technology and tested under quasi-static out-of-plane compression. The validated model was then employed to exploit optimal configuration of the N core and maximum load capacity of the panel at minimal weight. It was demonstrated that, due to non-uniform strut thickness, the hybrid structure exhibited stepwise deformation, *i.e.*, initial, subsequent and ultimate failures. Under the constraint of equal mass, the load capacity of either the hybrid or corrugated core is superior to the web core, while both the hybrid and web cores outperform the corrugated core in terms of active cooling capacity. For multifunctional applications, the proposed hybrid corrugated core possesses comprehensive thermal and mechanical advantages over conventional corrugated and web topologies.

## 1. Introduction

Lightweight structures with multi-functional attributes (*e.g.*, simultaneous load bearing and active cooling, simultaneous load bearing and sound attenuation, and simultaneous load bearing and energy absorption) are attractive in numerous engineering fields, including aerospace, transportation, nuclear engineering, and civil engineering [1]. For example, the scramjet of a hypersonic vehicle needs an actively cooled combustion chamber, which should dissipate the heat by cooling fluid and, simultaneously, bear the high pressure produced by deflagration [2,3]. Another example is the jet blast deflector (JBD) on the deck of aircraft carrier, which needs to withstand the high temperature of exhaust plume and bear the weight of the aircraft [4]. For

such applications, lightweight sandwich panels cored with fluid-through cellular metals are promising [5].

The vast variety of high porosity cellular metals may be categorized, in terms of topology, into three main types: (1) stochastic structures, such as metal foams [6,7] and fibril metals [8,9], (2) periodic lattices, such as corrugations [10,11], honeycombs [12,13] and pyramidal trusses [14,15], and (3) hybrid structures, such as foam-corrugation hybrid [16], honeycomb-corrugation hybrid [17], and X-lattice-honeycomb hybrid [18]. With stochastic topologies (including numerous processing-induced structural defects), metal foams have been demonstrated ideal for energy absorption [19,20] but not load bearing. While lattice structures (both two- and three-dimensional) are good at load bearing when subjected to, *e.g.*, compression [21],

---

---

**Nomenclature**

| | | | |
|---|---|---|---|
| $t_f$ | facesheet thickness | $I$ | inertial moment of strut cross-section |
| $t_o$ | oblique strut thickness | $A$ | cross-sectional area of strut |
| $t_l$ | left vertical strut thickness | $U$ | strain energy of strut |
| $t_r$ | right vertical strut thickness | $\sigma_Y$ | yielding strength |
| $\theta$ | oblique angle | $\sigma_{bl}, \sigma_{br}, \sigma_{bo}$ | |
| $h$ | sandwich height | | critical buckling stresses of left, right and oblique struts |
| $b$ | sandwich width | $k_l, k_r, k_o$ | elastic buckling coefficients of left, right and oblique struts |
| $\rho$ | core density | $p_i, p_s, p_f$ | initial, subsequent and ultimate failure loads |
| $Y_l, Y_r, Y_o$ | vertical loads that left, right and oblique struts bear | $B$ | connection efficiency factor |
| $X_o$ | horizontal load that oblique strut bears | $T_c$ | temperature of cooling water |
| $M_o$ | bending moment that oblique strut bears | $s$ | integral path |
| $\delta_l, \delta_r, \delta_o$ | vertical displacements at the ends of left, right and oblique struts | | |
| $\xi_o$ | horizontal displacement at the end of oblique strut | *Subscripts* | |
| $\alpha_o$ | rotation angle at the end of oblique strut | $l$ | left vertical strut |
| $p$ | out-of-plane pressure | $r$ | right vertical strut |
| $E$ | elastic modulus | $o$ | oblique strut |

---

bending [22] and shearing [23], their continuous and open channels also enable a cooling fluid to flow through [24]. By combing two or more different materials/structures, it has been demonstrated that the concept of hybrid material design can achieve superior mechanical performance in terms both specific stiffness/strength and specific energy absorption [25].

Based upon the fundamental topology of corrugations (*i.e.*, folded plates), hybrid structures filled with a number of materials have been proposed [16,17,26–30]. For example, using folding and laser welding technologies, Yan et al. produced a sandwich panel with aluminum foam-filled corrugated core and investigated its compressive [16] and bending [27] performances. The results showed that the strength and energy absorption capacity of the hybrid-cored panel was much greater than the sum of empty corrugated sandwich and aluminum foam alone. Subsequently, Han et al. [17] studied, both theoretically and experimentally, the out-of-plane compressive properties of a metallic trapezoidal corrugated sandwich filled with aluminum honeycomb and found superiority of the hybrid structure in terms of specific stiffness/strength and specific energy absorption (SEA). Actually, the hybrid honeycomb-corrugated core proposed by Han et al. [17] demonstrates the highest SEA among existing cores, as reviewed by Ha and Lu [1]. Also making use of the interstices in corrugations, Wei et al. [28] proposed an integrated thermal protection material based on C/SiC corrugated sandwich panel filled with glass wool, rock wool and other insulation materials, which could raise service temperature and reduce structural weight. Similarly, by filling alumina ceramics into the core of metallic corrugated sandwich panel, a novel composite bulletproof structure was constructed [29]: its ballistic performance characterized by ballistic limit and exit velocity of impact ejecta was significantly improved. By filling liquid damping materials into the pyramidal core, a hybrid composite pyramidal truss sandwich panel was constructed [30]: experimental results showed that such hybridization leads to enhanced damping loss efficiency.

The advantage of hybrid-cored sandwich constructions in mechanical properties stem mainly from the coupling enhancement effect between different core components. Han et al. [31] studied the cou-

pling effect between the folded plate (corrugation) and the inserted aluminum foam, and pointed out that support from foam on folded plate significantly elevated the plastic buckling strain of the sandwich. Similarly, strong interaction between honeycomb insertions and corrugated web was found to stabilize buckling and changed the crushing deformation mechanisms of both constituents, leading to enhanced strength and energy absorption [32].

In existing studies, hybrid-cored sandwich constructions based on inserting a different material into corrugations have no flow-through channels, thus restricts their applications in the scenario where active cooling is required in addition to load bearing. Therefore, as shown schematically in Fig. 1, the current study proposes a new hybrid-cored sandwich panel, termed herein as the N-type. The N-type hybrid core is formed by inserting I-type struts into the interstices of corrugated core, thus enabling cooling fluid to flow through each of its open channels. Our previous study [5] has shown that the heat dissipation performance of the N-type hybrid structure is superior to the conventional corrugated structure and almost identical to that of the web core structure (*i.e.*, I-core). Although the heat transfer performance of I-core is attractive [33], its mechanical performance is not, especially under out-of-plane compression and/or transverse shear. Therefore, in addition to heat dissipation, whether the proposed N-type hybrid structure has advantages in load capacity is another interesting topic.

For a N-type structure, in addition to the coupling effect between I struts and corrugated webs, the presence of I struts enables the structure to have constituent members with different thicknesses: a non-uniform distribution of wall thickness in the N-core is expected to cause competition and cooperation among the struts, thus influencing its load capacity significantly. In addition, the connection strength between the facesheet and the core is closely related to strut thickness [34], so how the introduction of I struts will influence the connection strength is another issue to be addressed. In the current study, an elastic–plastic theoretical model under out-of-plane compression load was stablished for the proposed N-type sandwich core, and the model predictions were compared with those calculated numerically using the method of finite elements (FE). Further validation were carried out
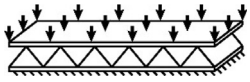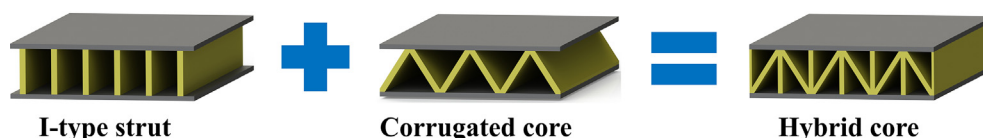


**Fig. 1.** Schematic of N-type hybrid core constructed by inserting I-type struts into interstices of conventional corrugations.

**Table 1**
Load type and core topologies considered in this study.

| Load type | Core topologies | | | |
|---|---|---|---|---|
| Out-of-plane compression | V-type | I-type | M-type | N-type |
|  |  |  |  |  |

by performing quasi-static out-of-plane compression experiment using alloy N-type sandwich sample fabricated via 3D printing. The validated analytical model was then employed to optimize the N-type hybrid core for superior mechanical performance, relative to conventional corrugated and web core topologies.

## 2. Problem description

Corrugated cores (named here as the V-type according to its cell topological shape) are extensively applied in a wide variety of fields, notably the packaging and transportation industry [35], while web cores (called herein as the I-type) including I girders and H beams are widely used in road and bridge construction [36]. In this study, as shown in Fig. 1 and Table 1, new hybrid corrugated cores, namely the N-type and the M-type, are proposed by combining the V- and I-type cores. The load type and core topologies considered in the study are listed in Table 1.

As the N-type core can be degenerated to other core types listed in Table 1, only the unit cell of N-type core was depicted for analysis in Fig. 2. There are two types of vertical strut in the N-type core: one meeting with the oblique strut at the top facesheet and the other meeting with the oblique strut at bottom facesheet. For easy to distinguish the two vertical struts, the former strut was referred to "left vertical strut", and the later as "right vertical strut" in the context below. Relevant geometric parameters include: facesheet thickness $t_f$, oblique strut thickness $t_o$, left vertical strut thickness $t_l$, right vertical strut thickness $t_r$, oblique angle $\theta$, and sandwich height $h$. With aim to develop lightweight structures, it is assumed that the struts are slender so that uniform stress distribution in each strut holds. Given the symmetry of the N-core, the solid cross-sectional area of each internal triangle (*i.e.*, open channel) in its unit cell is given by:

$$S_1 = \frac{(2h\cos\theta - t_o - t_f\cos\theta)^2}{8\sin\theta\cos\theta} - \frac{t_r(2h\cos\theta - t_o - t_f\cos\theta)}{4\cos\theta} + \frac{t_r^2}{8}\tan\theta \quad (1)$$

$$S_2 = \frac{(2h\cos\theta - t_o - t_f\cos\theta)^2}{8\sin\theta\cos\theta} - \frac{t_l(2h\cos\theta - t_o - t_f\cos\theta)}{4\cos\theta} + \frac{t_l^2}{8}\tan\theta \quad (2)$$

The total area of a single unit cell is:

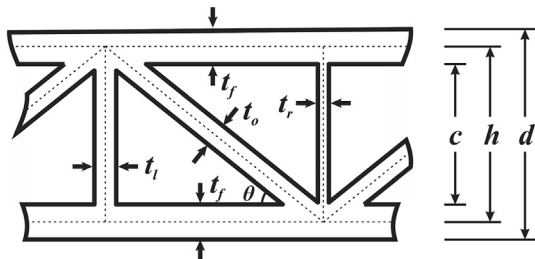$$S_0 = \frac{h(h + t_f)}{\tan\theta} \quad (3)$$



**Fig. 2.** Definition of geometrical parameters of the N-type hybrid structure.

The relative density of the N-core, $\rho$, can thus be calculated as:

$$\rho = 1 - \frac{S_1 + S_2}{S_0} = \frac{t_r^2 - 2t_f^2 + 16ht_f + t_l^2}{8h(h + t_f)}$$
$$- \frac{2\cos\theta((t_r + t_l)(t_f - 2h)\sin\theta - 4ht_o + 2t_ot_f) + 2t_o\sin\theta(t_r + t_l) + t_r^2 + 2t_o^2 + t_l^2}{8h\cos^2\theta(h + t_f)}$$

$$(4)$$

When $t_r = 0$, the structure degenerates to the M − core. It degenerates to the V-type when $t_l = t_r = 0$ and to the I-core when $t_o = 0$ and $t_l = t_r$. Therefore, analytical solutions obtained for the N-core are applicable to the other three cores.

## 3. Theoretical model

### 3.1. Initial failure

Fig. 3 shows schematically an N-core sandwich panel subjected to quasi-static, uniform out-of-plane compression $p$ at the top facesheet. The facesheets are assumed to be much stiffer than the core, so only transfer load to the core; the core members bear axial force, shear force and bending moment. The material make of the core is taken as ideal elastic–plastic so that, after initial failure of a strut, the supporting force of the strut does not change. As shown in Fig. 3, due to symmetry, it suffices to consider a unit cell for stress analysis.

When analyzing the force and moment balance of core struts, the load applied via facesheets to the struts can be equivalent to axial force, shear force and bending moment applied at the end of the struts. Suppose that the left and right vertical struts bear vertical forces $Y_l$ and $Y_r$, and the oblique struts bear horizontal forces $X_o$, vertical forces $Y_o$ and bending moments $M_o$. Therefore, the load matrix $\mathbf{F}$ of the struts can be expressed as:

$$\mathbf{F} = \begin{bmatrix} Y_l & Y_r & Y_o & X_o & M_o \end{bmatrix}^T \quad (5)$$

Correspondingly, the displacement matrix $\mathbf{\Delta}$ can be expressed as:

$$\mathbf{\Delta} = \begin{bmatrix} \delta_l & \delta_r & \delta_o & \xi_o & \alpha_o \end{bmatrix}^T \quad (6)$$

The subscripts $l$, $r$ and $o$ refer to the left vertical strut, the right vertical strut, and the oblique strut, respectively.

The strain energy stored in a strut can be calculated by:

$$U = \int \frac{M_s^2}{2EI}ds + \int \frac{F_N^2}{2EA}ds \quad (7)$$

where $M_s$ and $F_N$ are the bending moment and axial force of the strut, respectively, $E$ is the elastic modulus of material, $I$ and $A$ are the cross-sectional inertial moment and area of the strut, which satisfy:

$$M_s = 0, F_N = Y_l \quad \text{(for left vertical strut)} \quad (8)$$

$$M_s = 0, F_N = Y_r \quad \text{(for right vertical strut)} \quad (9)$$

$$M_s = M_o + Y_os\cos\theta - X_os\sin\theta, F_N$$
$$= Y_o\sin\theta + X_o\cos\theta \quad \text{(for oblique strut)} \quad (10)$$
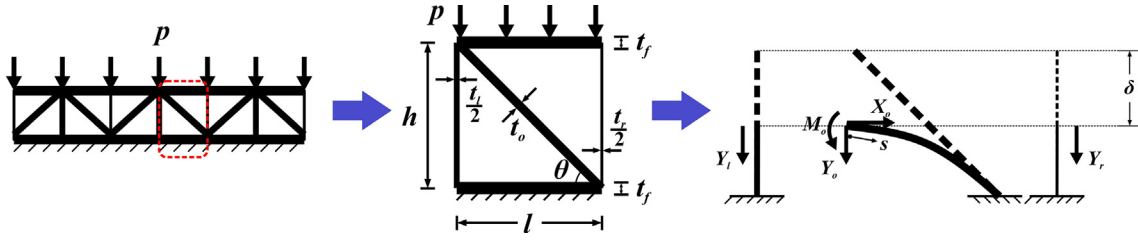
**Fig. 3.** Unit cell analysis of N-type core sandwich panel under uniform out-of-plane compression.

Upon substituting Eqs. (8–10) into Eq. (7), the strain energy $U_l$, $U_r$ and $U_o$ of the three strut types can be determined. The vertical displacement $\delta$, horizontal displacement $\xi$, and rotation angle $\alpha$ of each strut are related to the strain energy, as [37]:

$$\delta = \frac{\partial U}{\partial Y}, \xi = \frac{\partial U}{\partial X}, \alpha = \frac{\partial U}{\partial M} \tag{11}$$

The relationship between displacement $\mathbf{\Delta}$ and load $\mathbf{F}$ is obtained by simplifying the above formula, yielding:

$$\mathbf{\Delta} = \mathbf{DF} \tag{12}$$

where $\mathbf{D}$ is the compliance coefficient matrix, which can be derived from Eqs. (7–11), and its specific expression is given in Eq. (A1) of Appendix A. The above governing equation is subjected to corresponding displacement and force boundary conditions. For the oblique strut, its horizontal displacement $\xi_o$ and rotation angle $\alpha_o$ at the end are both null, while its vertical displacement $\delta_o$ is identical to that at the end of vertical struts. For the vertical struts, only vertical displacements are involved. The displacement boundary condition for all the struts can be written as:

$$\mathbf{L\Delta} = \mathbf{0} \tag{13}$$

where $\mathbf{L}$ is the coefficient matrix of displacement boundary condition, with its specific expression given in Eq. (A2). As to the force boundary condition, the vertical load sustained by all the struts is equal to the pressure of out-of-plane compression, yielding:

$$\mathbf{BF} = \frac{pbh}{\tan\theta} \tag{14}$$

where $\mathbf{B}$ is the coefficient matrix of force boundary condition, and its specific expression is given in Eq. (A3).

Equations (12–14) constitute a set of complete governing equations and boundary conditions for the load matrix $\mathbf{F}$, which can be solved as:

$$\mathbf{F} = \frac{bhp\cos\theta}{\sin\theta(h^2(t_l + t_r) + 2t_o\sin^3\theta(h^2 + t_o^2\cos^2\theta))} \begin{bmatrix} h^2t_l \\ h^2t_r \\ 2t_o\sin^3\theta(h^2 + t_o^2\cos^2\theta) \\ -2t_o\cos\theta\sin^2\theta(t_o^2\sin^2\theta - h^2) \\ -ht_o^3\sin^2\theta\cos\theta \end{bmatrix} \tag{15}$$

With reference to Fig. 3, let $\sigma_l$, $\sigma_r$ and $\sigma_o$ denote the maximum stresses of the left vertical strut, the right vertical strut and the oblique strut, respectively, which can be expressed using a stress matrix $\mathbf{\Sigma}$, as:

$$\mathbf{\Sigma} = \begin{bmatrix} \sigma_l & \sigma_r & \sigma_o \end{bmatrix}^T \tag{16}$$

The stress matrix $\mathbf{\Sigma}$ and the load matrix $\mathbf{F}$ satisfy:

$$\mathbf{\Sigma} = \mathbf{SF} \tag{17}$$

where $\mathbf{S}$ is the coefficient matrix of relationship between load and stress, given specifically in Eq. (A4). Substitution of Eq. (17) into Eq. (15) leads to:

$$\mathbf{\Sigma} = \frac{2h^3p\cos\theta}{\sin\theta(h^2(t_l + t_r) + 2t_o\sin^3\theta(h^2 + t_o^2\cos^2\theta))} \begin{bmatrix} 1 \\ 1 \\ \sin^2\theta \end{bmatrix} \tag{18}$$

It can be seen from Eq. (18) that the maximum stress of each strut increases linearly with out-of-plane pressure $p$, until elastic buckling or plastic yielding occurs:

$$\mathbf{\Sigma} < \begin{bmatrix} \min\{\sigma_{bl}, \sigma_Y\} \\ \min\{\sigma_{br}, \sigma_Y\} \\ \min\{\sigma_{bo}, \sigma_Y\} \end{bmatrix} \tag{19}$$

where $\sigma_Y$ is the yielding strength. The critical buckling stresses $\sigma_{bl}$, $\sigma_{br}$ and $\sigma_{bo}$ can be calculated as:

$$\sigma_{bl} = \frac{k_l\pi^2Et_l^2}{12h^2(1-\nu^2)}, \sigma_{br} = \frac{k_r\pi^2Et_r^2}{12h^2(1-\nu^2)}, \sigma_{bo} = \frac{k_o\pi^2Et_o^2\sin^2\theta}{12h^2(1-\nu^2)} \tag{20}$$

where $k_l$, $k_r$, $k_o$ are the elastic buckling coefficients depending on the restraint strength at both ends of each strut. Strictly speaking, the restraint strength depends on the relative thickness of the facesheet and the struts, and cannot be simplified using fixed or simply support. Determination of these elastic buckling coefficients will be discussed in Section 3.4.

Depending upon the type of failure mode, the initial failure load of the N-core hybrid structure calculated from Eqs. (18–20) is listed in Table A1 of Appendix A. As the sandwich is supported by three different kinds of struts in the core and is an indeterministic structure, the initial failure of a single strut does not mean that the structure reaches its peak load-bearing capacity, since the remaining struts can sustain additional load. After the initial failure of a single strut, the structure will progressively collapse until the second and third struts both fail, as detailed in the following sections in terms of subsequent failure and ultimate failure.

### 3.2. Subsequent failure

After the initial failure, the remaining struts can continue to support the external load $p$. Therefore, the load matrix, displacement matrix and coefficient matrix should be modified by excluding the elements corresponding to the damaged strut. Accordingly, the compliance relation, displacement and force boundary conditions become:

$$\tilde{\mathbf{\Delta}} = \tilde{\mathbf{D}}\, \tilde{\mathbf{F}} \tag{21}$$

$$\tilde{\mathbf{L}}\, \tilde{\mathbf{\Delta}} = \mathbf{0} \tag{22}$$

$$\tilde{\mathbf{B}}\, \tilde{\mathbf{F}} = \frac{pbh}{\tan\theta} - Y_i \tag{23}$$

where $Y_i$ is the vertical load sustained by the initially failed strut, which can be obtained by substituting the stress value in Table A1 into Eq. (15). Solving Eqs. (21–23) leads to the load matrix $\tilde{F}$. The maximum stress of the remaining struts can thence be derived, according to the updated relation between stress matrix and load matrix:

$$\tilde{\Sigma} = \tilde{S}\,\tilde{F} \qquad (24)$$

where the compliance matrix $\tilde{D}$, the displacement boundary coefficient $\tilde{L}$, the force boundary coefficient $\tilde{B}$ and the stress coefficient $\tilde{S}$ can be obtained by removing row or column elements in Eqs. (A1-A4) that correspond to the initial damaged strut, with specific expressions given in Table B1 in Appendix B. Based on Eq. (24), subsequent failure loads and the corresponding failure modes are presented in Table B2.

### 3.3. Ultimate failure

After the initial and subsequent failures, the N-cored sandwich can still support the load $p$ until the final strut is damaged, causing ultimate failure of the structure. At this point, the structure reaches its peak strength, which can be determined by:

$$Y_i + Y_j + Y_k = \frac{pbh}{\tan\theta} \qquad (25)$$

where $Y_i$, $Y_j$ and $Y_k$ are the vertical loads sustained by the initial, subsequent and ultimate failed struts, respectively. It can be seen from Eq. (25) that the order of *ijk* change arbitrarily. In other words, for each strut, if the failure mode is fixed, its failure sequence does not influence the ultimate failure load of the structure. Therefore, although there are in total 48 different ultimate failure modes, the ultimate failure load only has 8 different cases, as shown in Table C1 in Appendix C.

### 3.4. Elastic buckling coefficient

For a specific strut, the elastic buckling coefficients of Eq. (20), *i.e.*, $k_o$, $k_r$, $k_l$, can be determined by calculating the ratio of torsional stiffness provided by the facesheet and other two struts to the torsional stiffness of the strut itself.

For the left vertical strut as shown in Fig. 4(a), the total torsional stiffness $S_t$ imposed by the top facesheet and the two oblique struts at the top end is calculated by:

$$S_t = \frac{6EI_f}{l_f} + \frac{6EI_o}{l_o} \qquad 26$$

where $I_f\,(=bt_f^3/12)$ and $I_o\,(=bt_o^3/12)$ are the moment of inertia of the facesheet and oblique strut, respectively; $l_f\,(=h/\tan\theta)$ and $l_o\,(=h/\sin\theta)$ are separately the length of the facesheet and oblique strut.

The total torsional stiffness $S_b$ imposed by the bottom facesheet to the right vertical strut at its lower end is calculated by:

$$S_b = \frac{6EI_f}{l_f} \qquad 27$$

Then, ratios of the torsional stiffness of the left vertical strut itself to external torsional stiffness imposed at its top ($\eta_{l,t}$) and bottom ($\eta_{l,b}$) ends are calculated as:

$$\eta_{l,t} = \frac{EI_l}{l_l S_t} \qquad 28$$

$$\eta_{l,b} = \frac{EI_l}{l_l S_b} \qquad 29$$

It follows that the elastic buckling coefficient of the left vertical strut can be determined by [34]:

$$k_l = \frac{(0.4 + \eta_{l,t})(0.4 + \eta_{l,b})}{(0.2 + \eta_{l,t})(0.2 + \eta_{l,b})} \qquad 30$$

Upon combining Eqs. (26–30), $k_l$ can be expressed as a function of dimensionless thicknesses, as:

$$k_l = \frac{2.4\tan\theta\left(\frac{t_f}{t_l}\right)^3 + 2.4\sin\theta\left(\frac{t_o}{t_l}\right)^3 + 1}{1.2\tan\theta\left(\frac{t_f}{t_l}\right)^3 + 1.2\sin\theta\left(\frac{t_o}{t_l}\right)^3 + 1} \cdot \frac{2.4\tan\theta\left(\frac{t_f}{t_l}\right)^3 + 1}{1.2\tan\theta\left(\frac{t_f}{t_l}\right)^3 + 1} \qquad (31)$$

Similarly, the elastic buckling coefficients of the right vertical strut and oblique strut are obtained:

$$k_r = \frac{2.4\tan\theta\left(\frac{t_f}{t_r}\right)^3 + 2.4\sin\theta\left(\frac{t_o}{t_r}\right)^3 + 1}{1.2\tan\theta\left(\frac{t_f}{t_r}\right)^3 + 1.2\sin\theta\left(\frac{t_o}{t_r}\right)^3 + 1} \cdot \frac{2.4\tan\theta\left(\frac{t_f}{t_r}\right)^3 + 1}{1.2\tan\theta\left(\frac{t_f}{t_r}\right)^3 + 1} \qquad 32$$

$$k_o = \frac{\frac{1.2}{\sin\theta}\left(\frac{t_r}{t_o}\right)^3 + \frac{2.4}{\cos\theta}\left(\frac{t_f}{t_o}\right)^3 + 2.2}{\frac{0.6}{\sin\theta}\left(\frac{t_r}{t_o}\right)^3 + \frac{1.2}{\cos\theta}\left(\frac{t_f}{t_o}\right)^3 + 1.6} \cdot \frac{\frac{1.2}{\sin\theta}\left(\frac{t_l}{t_o}\right)^3 + \frac{2.4}{\cos\theta}\left(\frac{t_f}{t_o}\right)^3 + 2.2}{\frac{0.6}{\sin\theta}\left(\frac{t_l}{t_o}\right)^3 + \frac{1.2}{\cos\theta}\left(\frac{t_f}{t_o}\right)^3 + 1.6} \qquad 33$$

## 4. Experiment

### 4.1. Test sample fabrication based on 3D printing high strength aluminum alloy

In this study, high strength aluminum alloy powder developed by CRRC Industrial Academy was used to fabricate the test sample via 3D printing. To minimize the influence of boundary, the sample included two continuous unit cells, as shown in Fig. 6(a). The designed and actual geometric dimensions of the sample are listed in Table 2, which show that the three types of strut have non-uniform thickness, varying from 1 mm (right vertical strut), 2 mm (left vertical strut) to 3 mm (oblique strut).

To characterize the tensile properties of the high strength aluminum alloy, three dog-bone samples of identical size were fabricated, using the same 3D printing technology. Room temperature tensile tests were performed using standard servo-hydraulic test machine (MTS-858 Mini bionix, MTS Corporation, USA), at a nominal strain rate of $1 \times 10^{-3}\,\mathrm{s}^{-1}$ in accordance with ISO 6892–1:2009 [38]. Data reliability was improved by three repeated experiments. As shown in Fig. 5, the tensile stress is almost constant after yielding, which is consistent with the assumption of ideal elastic–plastic model. The elastic modulus
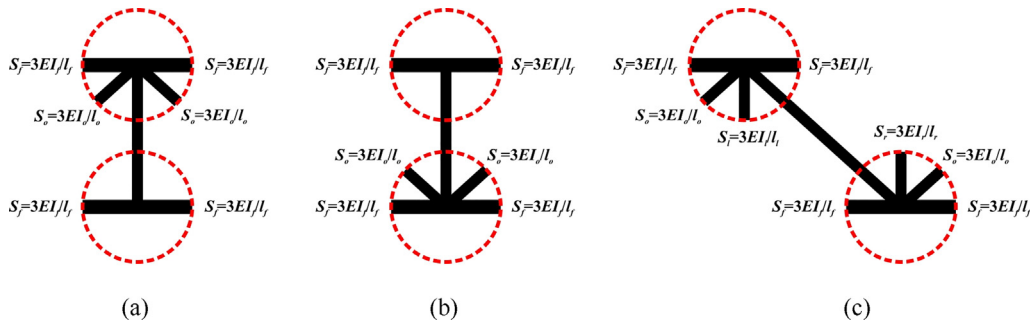


**Fig. 4.** Determination of torsional stiffness at top and bottom ends of each strut: (a) left vertical strut; (b) right vertical strut; (c) oblique strut.

**Table 2**
Geometric dimensions of N-type sandwich panel manufactured by 3D printing.

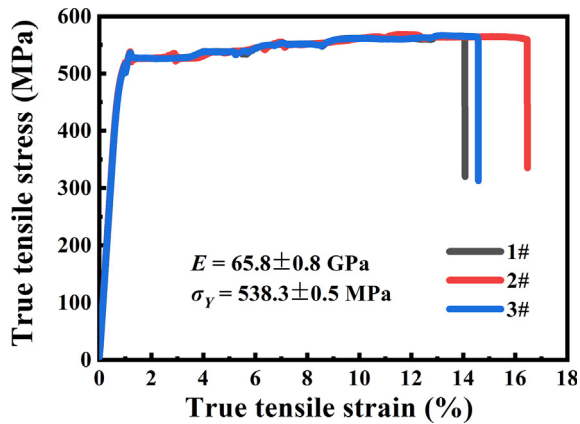|  | Length $L$ | Width $b$ | Height $h$ | Facesheet thickness $t_f$ | Oblique strut thickness $t_o$ | Left vertical strut thickness $tr$ | Right vertical strut thickness $tl$ |
|---|---|---|---|---|---|---|---|
| Design (mm) | 120.00 | 20.00 | 33.00 | 3.00 | 3.00 | 2.00 | 1.00 |
| Measured (mm) | 120.03 | 20.40 | 33.10 | 3.10 | 3.13 | 2.09 | 1.17 |



**Fig. 5.** True tensile stress versus true strain curves of 3D printed aluminum alloy.

($E$), yielding stress ($\sigma_Y$) and Poisson ratio ($\nu_s$) of the 3D printed aluminum alloy were measured to be 65.8 ± 0.8 GPa, 538.3 ± 0.5 MPa and 0.3, respectively.

### 4.2. Compression test

Quasi-static out-of-plane compression test of the fabricated sample was carried out on the hydraulic testing machine (MTS). The top and bottom facesheets were clamped with a pair of steel flange plates, the latter connected with the testing machine to transfer load and displacement, as shown in Fig. 6(b). At the beginning of test, the bottom flange plate was fixed, while the top flange plate exerted displacement loading, with a fixed rate of 1 mm/min. A computer-based data acquisition system was employed to record load and displacement during the test. The whole experimental process was monitored using a digital camera to record the deformation of test sample during compression.

### 5. Finite element modeling

Finite element simulations of N-type sandwich panels under quasi-static out-of-plane compression are carried out with ABAQUS/Explicit. A unit cell is taken to perform the simulations due to structural symmetry, and two rigid plates are used to model the puncher. Geometric imperfections induced during 3D printing are ignored. Four-node shell elements (S4R) having a size of 1 mm × 1 mm and five integration points through the thickness are used to model the facesheet and the core. Mesh sensitivity study was performed to ensure that the simulation results are independent of grid number. General contact was employed, with the Coulomb friction coefficient fixed at 0.2. Interfaces between the core and the facesheet were treated as perfectly bonded. Out-of-plane compressive loading was applied by moving the top rigid plate at a sufficiently low speed to mimic quasi-static loading [39]. The facesheet and the core are made of the high strength aluminum alloy, which is assumed isotropic and ideally elastic–plastic satisfying the von Mises J2 flow theory [40].

### 6. Results and discussion

#### 6.1. Initial, subsequent and ultimate failures

To further explore the initial, subsequent and ultimate failure phenomena, the out-of-plane compression process was simulated using the finite element method (FEM). The predictions were compared with experimental results in Fig. 7 in terms of force versus displacement curve as well as structural morphologies corresponding to initial, subsequent and ultimate failures. The three circled points on the curve correspond to the three failure morphologies. It is clear that there is significant difference among the three types of failure stress. The initial failure stress is therefore not the only index to characterize the load capacity of the structure, as it can still tolerate a great deal of structural damage after the initial failure.

As shown in Fig. 7, initial failure was caused by buckling of the left vertical struts and the two boundary vertical struts. Upon buckling, these vertical struts still provide certain support for the facesheet, but the growth rate of their axial stresses slightly dropped relative to the totally elastic stage. As the load was further increased, the right vertical strut yielded, corresponding to point 2 of the force versus displacement curve. This led to further decline in stress growth rate between points 2 and 3. Ultimate failure occurred at point 3, when the oblique strut started to yield. After the ultimate failure, the load capacity of the whole sandwich decreased rapidly. Overall, the FEM results were in good agreement with the experimental results, especially the trend of slope change in stress versus strain curve and the deformed morphologies of vertical/oblique struts.
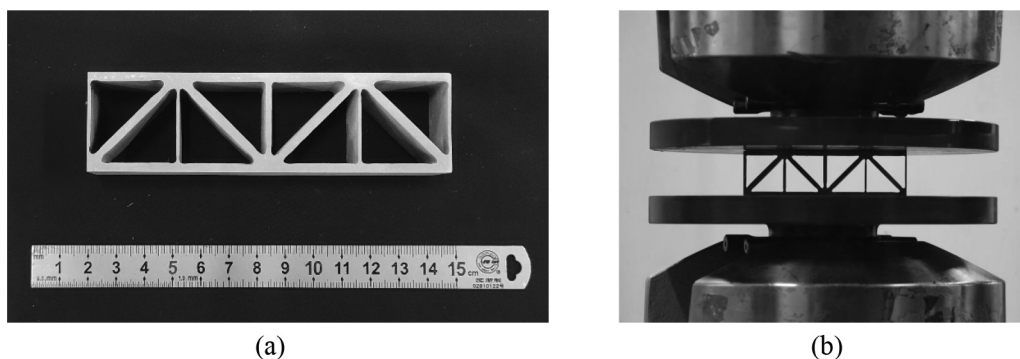


(a)

(b)

**Fig. 6.** Test sample and experimental apparatus: (a) 3D printed N-core sandwich; (b) compression test.
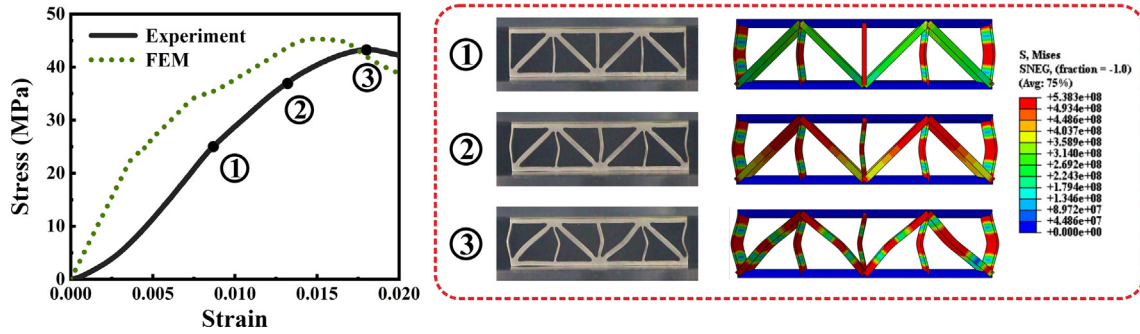
**Fig. 7.** Comparison of experimental and simulated stress versus strain curve and deformation morphologies at initial failure (point 1), subsequent failure (point 2) and ultimate failure (point 3) for N-type hybrid structure subjected to out-of-plane compression.

### 6.2. Validation of the theoretical model

Next, the validated FEM model was used to verify the theoretical model. Fig. 8 depicts the initial, subsequent and ultimate failure loads of the N-type hybrid structure as functions of oblique strut thickness ($t_o / h$), with other geometric parameters fixed at $t_f / h = 0.04$, $t_r / h = 0.01$, $t_l / h = 0.04$, $\theta = 45°$. The numerical results agreed excellently well with the theoretical predictions, thus validating the theoretical model developed in the present study. Both models predicted a big gap between the initial failure stress and the final failure stress, regardless the thickness of the oblique strut. That is to say, it is not comprehensive to use a single initial failure load to characterize the load capacity of an N-type structure, for it still has great load-bearing capacity after initial failure.

### 6.3. Parametrical study

As discussed in the previous sections, the failure process of an N-type hybrid structure can be divided into three stages, *i.e.*, initial, subsequent and ultimate failure, wherein each failure stage may involve either the buckling or yielding of top/right vertical struts and oblique struts. To characterize such complex failure conditions, a graphic representation rule was designed to help identifying the failure mode (elastic buckling versus plastic yielding) and the failure stage (initial, subsequent, ultimate failure). As shown in Table 3, different shapes were used to distinguish different failure mode, *e.g.*, bending strut represents elastic buckling, while serrated strut represents plastic yielding. Four different colors, *i.e.*, black, blue, green and red, were adopted to represent no failure, initial failure, subsequent failure and ultimate failure, respectively.
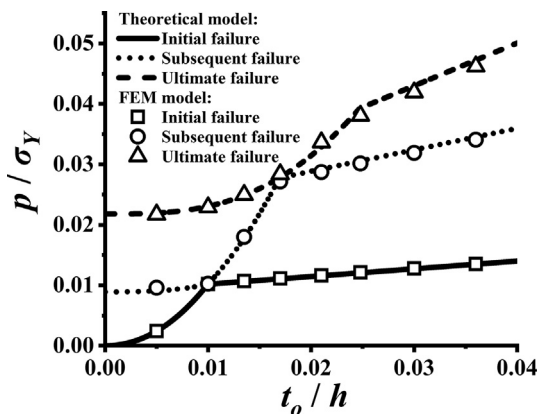


**Fig. 8.** Initial, subsequent and ultimate failure loads of N-type hybrid structure plotted as functions of oblique strut thickness: comparison between theoretical model predictions and FEM results ($t_f / h = 0.04$, $t_r / h = 0.01$, $t_l / h = 0.04$, $\theta = 45°$).

For a given N-type hybrid structure subjected to out-of-plane compression, there are in total $6 \times 4 \times 2 = 48$ possible combinations of failure route (including failure mode and failure stage). For example, which strut will fail first and what is the corresponding failure mode? Is there an optimal failure route for maximum load capacity under the condition of constant structural mass? Usually, as the thinnest strut will first fail, failure route can certainly be tailored by varying the geometric parameters. There are in total five geometric parameters, including the facesheet thickness $t_f$, the oblique strut thickness $t_o$, the right vertical strut thickness $t_r$, the left vertical strut thickness $t_l$ and the oblique angle $\theta$. Under equal mass condition, these geometric parameters are not completely independent of each other: there are only four independent parameters, as indicated in Eq. (4). Next, effects of each geometrical parameters will be analyzed on the premise of equal mass, *i.e.*, equal relative density.

#### 6.3.1. Influence of thickness ratio between right and left vertical struts

Fig. 9 plotted the initial and ultimate failure loads as functions of the thickness ratio ($t_r / t_l$) between right and left vertical struts, with $t_f / h = 0.02$, $t_o / h = 0.01$, $\theta = 45°$ and $\rho = 0.1$. Typical failure routes corresponding to different thickness ratios were illustrated in the figure. As the right vertical strut became thicker and the left vertical strut became thinner, the initial failure load rose first and then decreased, peaking near $t_r / t_l = 1$. The right vertical strut buckled first when $t_r / t_l$ is small, but the left vertical strut buckled first when $t_r / t_l$ is big. In contrast, when $t_r / t_l$ is moderate, the left and right vertical struts both first yielded. As the predicted ultimate failure load of the N-type hybrid structure was almost constant, its load-bearing capacity is insensitive to $t_r / t_l$ under equal mass. Strictly speaking, the load-bearing capacity is maximized when the two vertical struts have identical thickness, *i.e.*, the structure is symmetrical. Here, it is recalled that the symmetrical web core (*i.e.*, $t_r = t_l$) is a popular topology for sandwich construction [41].

When the thickness ratio becomes infinitely small (or large), *i.e.*, $t_r / t_l \to 0$ (or $t_r / t_l \to \infty$), the N-type structure is reduced to the M-type. The results of Fig. 9 showed that, under the condition of equal mass, the ultimate failure load of the M-type structure is almost equal to that of the N-type.

#### 6.3.2. Influence of oblique strut thickness

To quantify the influence of oblique strut thickness, the remaining geometric parameters were all fixed. The thickness ratio $t_r / t_l$ was fixed to be unit, corresponding to the largest load capacity of the N-type structure as discussed in the previous section. Two parameter combinations for the facesheet thickness, oblique angle and relative density were selected: $t_f / h = 0.02$, $\theta = 45°$, $\rho = 0.1$ and $t_f / h = 0.02$, $\theta = 85°$, $\rho = 0.3$. Corresponding failure loads plotted as functions of dimensionless thickness of the oblique strut ($t_o / t_r$) were presented in Fig. 10 (a) and (b), respectively. As the oblique strut was

**Table 3**
Graphic representation of failure route including failure mode and failure stage.

| Failure mode | Elastic buckling | | Plastic yielding | |
|---|---|---|---|---|
| Failure stage | No failure | Initial failure | Subsequent failure | Ultimate failure |
| Examples | Initial failure | Subsequent failure | Ultimate failure | Legend |
| | Yielding of oblique strut | – | – | |
| | Buckling of right vertical strut | Yielding of left vertical strut | – | |
| | Buckling of oblique strut | Buckling of right vertical strut | Yielding of left vertical strut | |
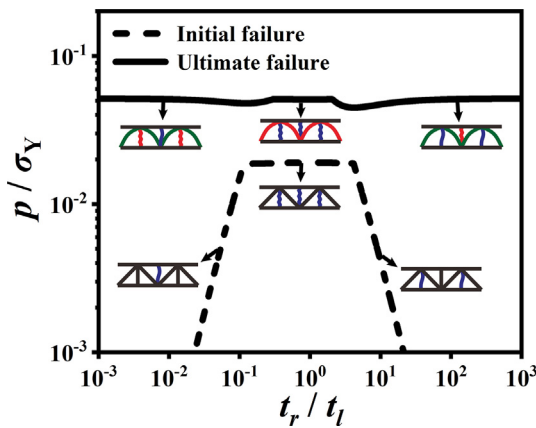


**Fig. 9.** Influence of thickness ration between right and left vertical struts on initial and ultimate failure loads of N-type hybrid structure.

changed from thin to thick, *i.e.*, the two vertical struts varied from thick to thin under given mass of the structure, the initial failure load rose first and then decreased, peaking near $t_o / t_r = 0.5$ (point A). Here, yielding of the two vertical struts was the initial failure mode. For a structure with small oblique angle and low relative density, *e.g.*, $\theta = 45°$, $\rho = 0.1$ as shown in Fig. 10 (a), the ultimate failure load decreased slowly as $t_o / t_r$ was increased. In contrast, it rose gradually in the case of big oblique angle and high relative density as shown in Fig. 10 (b) for $\theta = 85°$ and $\rho = 0.3$.
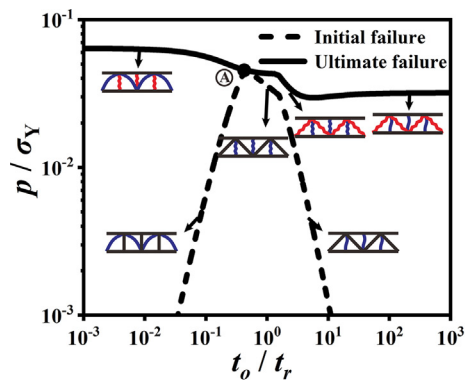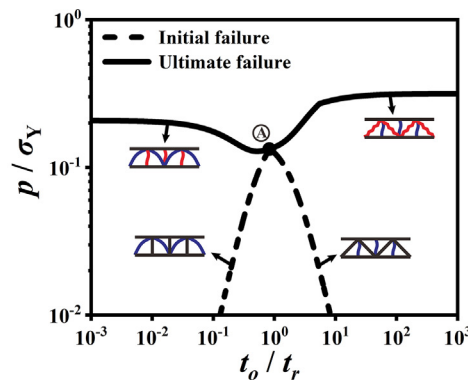
As $t_o / t_r$ was increased, the gap between the loads of ultimate failure and initial failure first decreased and then increased, meaning that the initial failure is more likely to occur when a strut is much thinner than the others, similar to the observation in Fig. 9. The ultimate failure load is mainly dependent upon the mass of the structure, thus the variation of final load is relatively small compared to the initial load. A special point A in Fig. 10 is noted, where the initial and ultimate failure loads are equal and the initial load peaks. At point A, the three struts in a unit cell failed simultaneously. This special point is also a demarcation point of failure mode, which will be discussed in the next section.

The limiting cases of $t_o / t_r \to 0$ and $t_o / t_r \to \infty$ correspond to the conventional I-type (or I-beam) and V-type (corrugated) structures, respectively. Therefore, for both limiting cases, the structure exhibits only one failure stage. Under the condition of equal mass, the failure load of the I-type structure is nearly 100% higher than that of the V-type in the case of small oblique angle and low relative density, as shown in Fig. 10(a). However, in the case of large oblique angle and high relative density as shown in Fig. 10(b), the situation is completely reversed: the V-type structure has a load capacity 51.7% higher than that of the I-type. It is noted that, for a fixed set of parameter combinations in Fig. 10, the load-bearing capacity of the N-type structure is not as good as that of the conventional I- and V-type structures of equal mass, for the N-type structure with more design parameters is yet optimized. In Section 7, a global parametric optimization of the N-type structure will be performed and the performance of the optimized structure will be compared with conventional structures.



(a)



(b)

**Fig. 10.** Influence of oblique strut thickness on initial and ultimate failure loads of N-type hybrid structure with (a) $\theta = 45°$, $\rho = 0.1$, $t_r / t_l = 1$ and (b) $\theta = 85°$, $\rho = 0.3$, $t_r / t_l = 1$.

### 6.3.3. Influence of oblique angle

With $t_o = t_r = t_l$, $t_f / h = 0.02$ and $\rho = 0.1$, the inclination angle of the oblique strut was varied to examine its effects on initial and ultimate failure loads of N-type hybrid structures under equal mass. Fig. 11 showed that the initial and ultimate failure loads both first increased and then decreased as the inclination angle was increased from 0 to 90°. The optimal inclination angle was ~ 52°, where both the initial and ultimate loads peaked. Meanwhile, with increasing
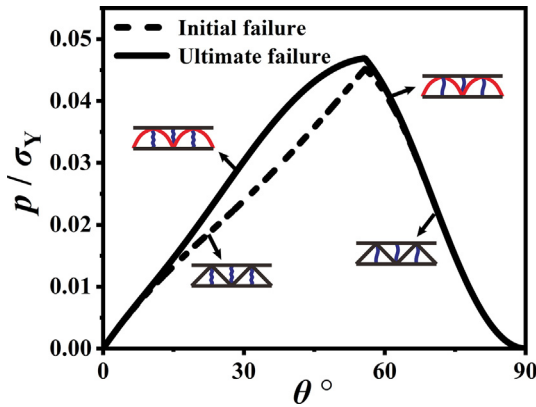


**Fig. 11.** Influence of inclination angle on initial and ultimate failure loads of N-type hybrid structure.
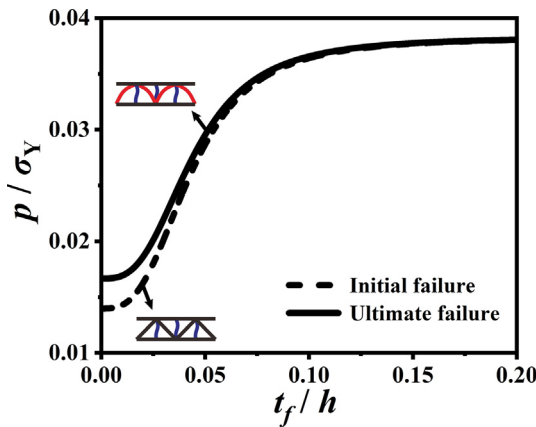


**Fig. 12.** The influence of facesheet thickness on initial and ultimate failure loads of the N-type hybrid structure.

inclination angle, the initial failure mode changed from yielding to buckling of the two vertical struts, while the ultimate failure mode was always buckling of the oblique strut.

### 6.3.4. Influence of facesheet thickness

It was assumed that the facesheets do not suffer bending moment but only transfer load to the core struts in the theoretical model. However, the facesheets provide mechanical supports to the struts, and the strength at the connection between the facesheet and struts affects the torsional stiffness and buckling resistance of the core struts. According to Eqs. (31–33), the strength at the connection is determined by thickness ratios of facesheet to the three struts, *i.e.*, $t_f / t_l$, $t_f / t_r$, $t_f / t_o$. Hence it is necessary to discuss the influence of facesheet thickness on the overall load capacity of sandwich panel. With all of the core geometric parameters kept constant, *e.g.*, $t_o / h = 0.04$, $t_r / h = 0.04$, $t_l / h = 0.04$ and $\theta = 45°$, Fig. 12 shows the initial and ultimate failure loads of N-type hybrid structure subject to the varying of facesheet thickness ($t_f / h$). It can be found that the initial and ultimate failure loads both first increase rapidly as increasing the facesheet thickness, and approach asymptotic when the facesheet thickness is higher than a critical value, *e.g.*, $t_f / h > 0.1$.

### 6.4. Failure maps

The effects of geometric parameters on initial and ultimate failure loads were quantified in the previous section, under the condition of equal mass. This section focused on the construction of failure maps, with each geometric parameter varying in a wide range. Since the influence of facesheet thickness $t_f$ on out-of-plane compression characteristics tends to be asymptotic if $t_f$ is larger than a critical value, for simplicity it was fixed at $t_f / h = 0.1$ (beyond the critical value). There are thus only four independent geometric parameters, *i.e.*, oblique strut thickness $t_o$, left vertical strut thickness $t_l$, right vertical strut thickness $t_r$, oblique angle $\theta$ and sandwich height $h$. In addition, as discussed in the previous section, the N-type structure exhibited high load capacity if the two vertical struts have the same thickness ($t_r = t_l$) under the condition of equal mass. Therefore, the thickness ratio $t_r / t_l$ was fixed at unity to further reduce the number of variables in the failure map. The map of initial and ultimate failure modes can thence be drawn using three parameters (*i.e.*, $t_o / h$, $t_r / h$ and $\theta$), as shown in Fig. 13(a).

Theoretically, if the two vertical struts are assumed identical, there are in total 4 (initial failure) × 2 (ultimate failure) = 8 different types of failure mode. However, the table in Fig. 13 showed that only 6 failure modes existed in reality. Two possible failure modes were absent,
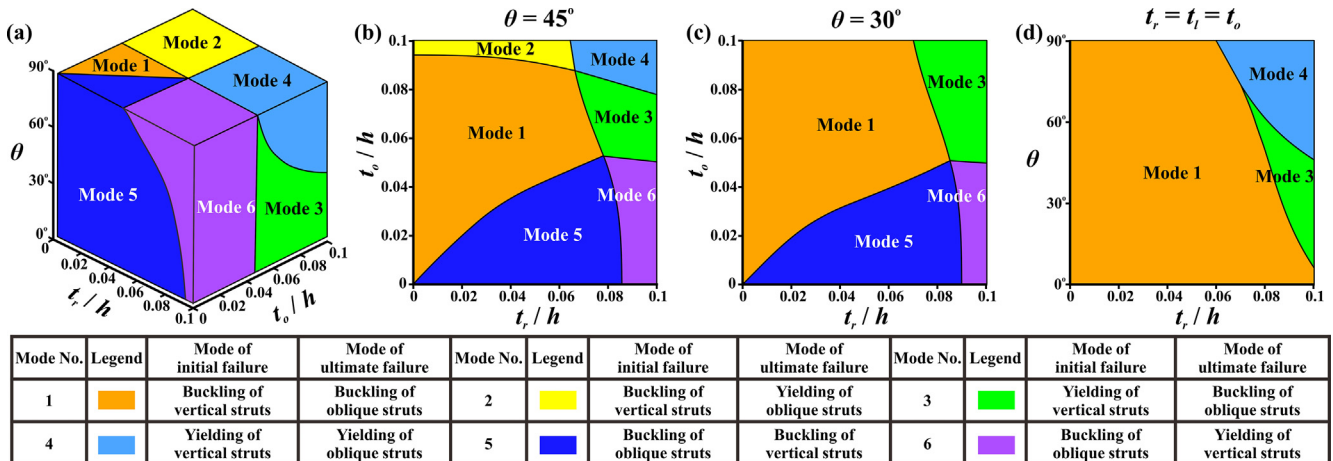


| Mode No. | Legend | Mode of initial failure | Mode of ultimate failure | Mode No. | Legend | Mode of initial failure | Mode of ultimate failure | Mode No. | Legend | Mode of initial failure | Mode of ultimate failure |
|---|---|---|---|---|---|---|---|---|---|---|---|
| 1 | | Buckling of vertical struts | Buckling of oblique struts | 2 | | Buckling of vertical struts | Yielding of oblique struts | 3 | | Yielding of vertical struts | Buckling of oblique struts |
| 4 | | Yielding of vertical struts | Yielding of oblique struts | 5 | | Buckling of oblique struts | Buckling of vertical struts | 6 | | Buckling of oblique struts | Yielding of vertical struts |

**Fig. 13.** Failure map of N-type hybrid structure showing its initial and ultimate failure modes: (a) 3-D failure map subject to changes of $t_r$, $t_o$ and $\theta$; slices of 3-D failure map with $\theta$ fixed at (b) 45° and (c) 30° (c), as well as with (d) $t_r = t_l = t_o$ (d). For the plotting, $t_f / h = 0.1$ and $t_r = t_l$.

*i.e.*, (oblique strut yielding, vertical strut buckling) and (oblique strut yielding, vertical strut yielding), where the first and second components in the bracket represented the initial and ultimate failure modes, respectively. This occurred because yielding of the vertical strut ($p_{vy}$) is always prior to yielding of the oblique strut ($p_{oy}$), the latter attributed to the fact that $p_{oy} / p_{vy} = 1 / \sin 2\theta > 1$ always holds (more details are referred to Table A1). Therefore, yielding of the oblique strut as an initial failure would never happen.

To facilitate the study of failure modes, the 3-D failure map of Fig. 13(a) was sliced at fixed $\theta$ of 45° and 30° as well as at $t_r = t_l = t_o$, as shown in Fig. 13(b-d). When the struts are relatively thin, the structure is more likely to buckle rather than yield, *e.g.*, Mode 1 and Mode 5 failure as shown in Fig. 13(b) and (c), and the smaller the oblique angle is, the more likely the structure is to buckle rather than yield. As shown in Fig. 13(d), if all the struts have identical thickness, the vertical strut always fails prior to the oblique strut regardless of its oblique angle. That is, the load capacity of the oblique strut is always higher than that of the vertical strut having identical thickness.

# 7. Optimization

## 7.1. Definition of optimization problem

It can be seen from Tables A1 and C1 that, with material make fixed, the initial and ultimate failure loads of an N-type hybrid structure are functions of five geometric parameters, namely:

$$p_i = f_1\left(\frac{t_f}{h}, \frac{t_o}{h}, \frac{t_r}{h}, \frac{t_l}{h}, \theta\right) \qquad 34$$

$$p_f = f_2\left(\frac{t_f}{h}, \frac{t_o}{h}, \frac{t_r}{h}, \frac{t_l}{h}, \theta\right) \qquad 35$$

According to Eqs. (1–4), the relative density of the structure is also a function of geometric parameters:

$$\rho = g\left(\frac{t_f}{h}, \frac{t_o}{h}, \frac{t_r}{h}, \frac{t_l}{h}, \theta\right) \qquad 36$$

The optimization objective is to find the maximum ultimate failure load under the constraint of equal mass:

$$\begin{aligned} &\max p_f \\ &s.t. \rho = \rho_0 \\ &10^{-3} \leqslant t_o/t_r \leqslant 10^3 \\ &10^{-3} \leqslant t_r/t_l \leqslant 10^3 \\ &0° < \theta < 90° \end{aligned} \qquad 37$$

where the ranges of thickness ratios and inclination angle were restrained to ensure that the struts are not too thin or too thick and the inclination is meaningful in engineering practice. The exhaustive search method was adopted to solve the above nonlinear optimization problem, with the multi-core parallel algorithm adopted to speed up the solution process [42].

## 7.2. Comparison of different optimal structures

For N-/M-/V-/I-type sandwich structures, Fig. 14(a) presents their optimized ultimate failure loads as functions of core relative density. Since failure mode is dependent upon relative density, the curve in Fig. 14(a) can be divided into three regions according to the relative density: elastic zone, transition zone and plastic zone. In the elastic zone with low relative density ($0 < \rho < 0.06$), the initial, subsequent and ultimate failure modes are all elastic buckling. In the plastic zone with high relative density ($0.13 < \rho < 0.5$), the initial, subsequent and ultimate failure mode are all plastic yielding. In the transition zone with intermediate relative density ($0.06 < \rho < 0.13$), elastic buckling and plastic yielding coexist.

As shown in Fig. 14(a), at a given relative density, the N- and M-type structures exhibited a higher load capacity than the V- and I-type structures. The I-type structure is better than the V-type at low densities ($\rho < 0.06$), while the reverse holds at high densities ($\rho > 0.18$); at moderate densities, the two structures have similar performance. Although the load capacity of the N-type is close to the M-type and slightly higher than the V-type, it had previously been demonstrated that the N-type structure possesses significantly higher convective cooling efficiency than both M- and V-type structures, due to relatively uniform distribution of flow channels in the N-type [5]. Therefore, the N-type structure has comprehensive advantages over other structures for multifunctional applications demanding simultaneous load-bearing and active cooling.

To show how the topological characteristics of each optimized structure vary with core relative density, Fig. 14(b) plotted the optimal thickness of oblique strut $t_o / h$ and optimal inclination angle $\theta$ as functions of relative density for the optimized V-type structure. Within the low density zone where buckling failure dominates, the optimal thickness of oblique strut increases with relative density, while its optimal inclination angle is almost constant (~54°). Within the transition and plastic zones, the optimal thickness no longer increases with increasing relative density, but the optimal inclination angle increases rapidly, approaching 90° in the high relative density zone where yielding failure dominates. In conclusion, in the high density zone, the V-type structure tends to obtain maximum load capacity with denser arrangement of struts having constant thickness.

Similarly, Fig. 14(c) and (d) displayed how the optimal geometric parameters of optimized M- and N-type structures vary with relative density. For both structures, in the elastic buckling zone the optimal inclination angle increases rapidly with increasing relative density, and the optimal thickness of vertical strut is much greater than the oblique strut, *i.e.*, $t_l \ll t_o$. This indicates that, in the low relative density zone, the optimized M- and N-type structures are closer to the I-type structure. For both structure, in the plastic yielding zone, the optimal inclination angle increases slowly to 90°, while the optimal thickness of oblique and vertical struts remains constant as the relative density is increased, similar to the V-type structure. Finally, it is worth noting that for the N-type structure, the optimal thickness of the other vertical strut tends to 0, *i.e.*, $t_r \square t_l$, which means that the optimal N-
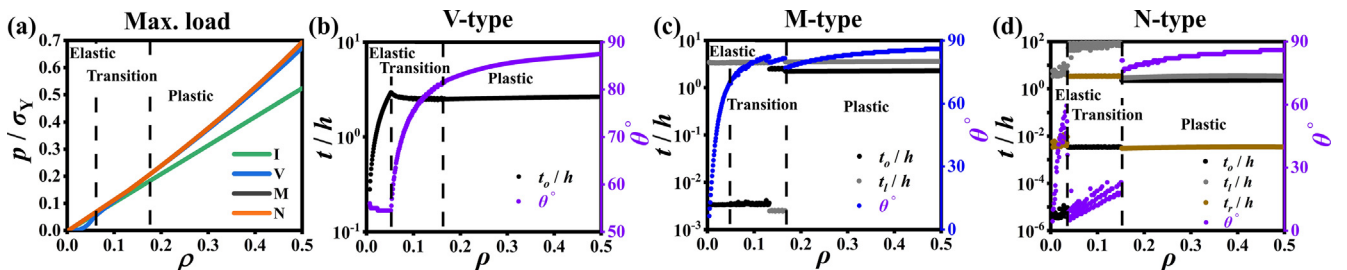


**Fig. 14.** Maximum ultimate failure load (a) and corresponding topological characteristics (b-d) of optimized N-/M-/V-/I-type sandwich structures having varying core relative densities.

type structure is close to the M-type structure in the high relative density zone.

## 8. Conclusion

The out-of-plane compression behavior of a novel hybrid-cored sandwich panel was investigated using theoretical modeling, experimental measurement and numerical simulation. The proposed hybrid core, termed as the N-type, was constructed by combining the conventional corrugated core (V-type) with the web core (I-type). An analytical model was developed to predict its failure mode and load capacity, which was validated by numerical simulations with the method of finite elements and experimental measurements. The validated analytical model was subsequently adopted to optimize its geometric parameters under the constraint of equal mass. It was found that the hybrid structure fails stepwise under out-of-plane compression, causing three segments with different slopes in the stress–strain curve, corresponding to initial, subsequent and ultimate failures, respectively. The failure order and failure mode (buckling versus yielding) depend on the combination of geometric parameters, so the failure map of the structure can be tailored by adjusting the geometrical parameters. The exhaustive search method was used to find the optimal combination of geometric parameters. The optimized failure load of the hybrid structure was compared with competing structures of equal mass. It was demonstrated that the proposed structure inherits the mechanical and thermal attributes of V- and I-type structures, thus promising for multifunctional applications requiring simultaneous load-bearing and active cooling at minimal mass.

## Declaration of Competing Interest

The authors declare that they have no known competing financial interests or personal relationships that could have appeared to influence the work reported in this paper.

## Acknowledgements

## Appendix A. Supplementary data

Supplementary data to this article can be found online at https://doi.org/10.1016/j.compstruct.2021.114222.

## References

[1] Ha NS, Lu G. Thin-walled corrugated structures: A review of crashworthiness designs and energy absorption characteristics. Thin-Walled Struct 2020;157:106995. https://doi.org/10.1016/j.tws.2020.106995.

[2] Valdevit L, Vermaak N, Zok F W, et al. A materials selection protocol for lightweight actively cooled panels. J Appl Mechan; 2008, 75: 061022.

[3] Vermaak N, Valdevit L, Evans A, Zok F, McMeeking R. Implications of shakedown for design of actively cooled thermostructural panels. J Mechan Mater Struct 2011;6(9-10):1313–27.

[4] Li X, Feng SS, Kim T, Lu TJ. Numerical investigation of forced convection in pin/plate-fin heat sinks heated by impinging jet using porous medium approach. Int J Numer Meth Heat Fluid Flow 2013;23(1):88–107.

[5] Sun S, Feng S, Zhang Q, Lu TJ. Forced convection in additively manufactured sandwich-walled cylinders with thermo-mechanical multifunctionality. Int J Heat Mass Transf 2020;149:119161. https://doi.org/10.1016/j.ijheatmasstransfer.2019.119161.

[6] Seitzberger M, Rammerstorfer FG, Gradinger R, Degischer HP, Blaimschein M, Walch C. Experimental studies on the quasi-static axial crushing of steel columns filled with aluminium foam. Int J Solids Struct 2000;37(30):4125–47.

[7] Lu TJ, Stone HA, Ashby MF. Heat transfer in open-cell metal foams. Acta Mater 1998;46(10):3619–35.

[8] Yuranov I, Kiwi-Minsker L, Renken A. Structured combustion catalysts based on sintered metal fibre filters. Appl Catal B 2003;43(3):217–27.

[9] Sun J, Hu Z, Li J, Zhang H, Sun ChenCheng. Thermal and mechanical properties of fibrous zirconia ceramics with ultra-high porosity. Ceram Int 2014;40(8):11787–93.

[10] Rejab MRM, Cantwell WJ. The mechanical behaviour of corrugated-core sandwich panels. Composites: Part B-Engineering 2013;47:267–77.

[11] Zhao Z-y, Han B, Wang X, Zhang Q-C, Lu TJ. Out-of-plane compression of Ti-6Al-4V sandwich panels with corrugated channel cores. Mater Des 2018;137:463–72.

[12] Côté F, Deshpande VS, Fleck NA, Evans AG. The out-of-plane compressive behavior of metallic honeycombs. Mater Sci Eng, A 2004;380(1-2):272–80.

[13] Lu TJ. Heat transfer efficiency of metal honeycombs. Int J Heat Mass Transf 1999;42(11):2031–40.

[14] Wu Q, Gao Y, Wei X, Mousanezhad D, Ma Li, Vaziri A, et al. Mechanical properties and failure mechanisms of sandwich panels with ultra-lightweight three-dimensional hierarchical lattice cores. Int J Solids Struct 2018;132-133:171–87.

[15] Wu Q, Vaziri A, Asl ME, Ghosh R, Gao Y, Wei X, et al. Lattice materials with pyramidal hierarchy: Systematic analysis and three dimensional failure mechanism maps. J Mech Phys Solids 2019;125:112–44.

[16] Yan LL, Yu B, Han B, Chen CQ, Zhang QC, Lu TJ. Compressive strength and energy absorption of sandwich panels with aluminum foam-filled corrugated cores. Compos Sci Technol 2013;86:142–8.

[17] Han B, Qin K, Yu Bo, Wang Bo, Zhang Q, Lu TJ. Honeycomb-corrugation hybrid as a novel sandwich core for significantly enhanced compressive performance. Mater Des 2016;93:271–82.

[18] Yan H, Zhang Q, Chen W, Xie G, Dang J, Lu TJ. An X-lattice cored rectangular honeycomb with enhanced convective heat transfer performance. Appl Therm Eng 2020;166:114687. https://doi.org/10.1016/j.applthermaleng.2019.114687.

[19] Peroni L, Avalle M, Peroni M. The mechanical behaviour of aluminium foam structures in different loading conditions. Int J Impact Eng 2008;35(7):644–58.

[20] Sriram R, Vaidya UK, Kim JE. Blast impact response of aluminum foam sandwich composites. J Mater Sci 2006;41(13):4023.

[21] Gibson LJ, Ashby MF. Cellular solids: structure & properties. Cambridge: Cambridge University Press; 1997.

[22] Valdevit L, Hutchinson JW, Evans AG. Structurally optimized sandwich panels with prismatic cores. Int J Solids Struct 2004;41(18-19):5105–24.

[23] Côté F, Deshpande VS, Fleck NA, Evans AG. The compressive and shear responses of corrugated and diamond lattice materials. Int J Solids Struct 2006;43(20):6220–42.

[24] Lu TJ, Xu F, Wen T, editors. Thermo-Fluid Behaviour of Periodic Cellular Metals. Berlin, Heidelberg: Springer Berlin Heidelberg; 2013.

[25] Ashby MF, Bréchet YJM. Designing hybrid materials. Acta Mater 2003;51(19):5801–21.

[26] Dayyani I, Shaw AD, Saavedra Flores EI, Friswell MI. The mechanics of composite corrugated structures: a review with applications in morphing aircraft. Compos Struct 2015;133:358–80.

[27] Yan LL, Han B, Yu B, Chen CQ, Zhang QC, Lu TJ. Three-point bending of sandwich beams with aluminum foam-filled corrugated cores. Mater Des 2014;60:510–9.

[28] Wei K, Wang K, Cheng X, Peng Y, Li M, Yang X. Structural and thermal analysis of integrated thermal protection systems with C/SiC composite cellular core sandwich panels. Appl Therm Eng 2018;131:209–20.

[29] Wadley HNG, O'Masta MR, Dharmasena KP, Compton BG, Gamble EA, Zok FW. Effect of core topology on projectile penetration in hybrid aluminum/alumina sandwich structures. Int J Impact Eng 2013;62:99–113.

[30] Yang J-S, Ma Li, Schmidt R, Qi Ge, Schröder K-U, Xiong J, et al. Hybrid lightweight composite pyramidal truss sandwich panels with high damping and stiffness efficiency. Compos Struct 2016;148:85–96.

[31] Han B, Yan L, Yu Bo, Zhang Q, Chen C, Lu T. Collapse mechanisms of metallic sandwich structures with aluminum foam-filled corrugated cores. J Mechan Mater Struct 2014;9(4):397–425.

[32] Zhang Z-J, Zhang Q-C, Zhang D-Z, Li Y, Jin F, Fang D-N. Enhanced mechanical performance of brazed sandwich panels with high density square honeycomb-corrugation hybrid cores. Thin-Walled Struct 2020;151:106757. https://doi.org/10.1016/j.tws.2020.106757.

[33] Zhao CY, Lu TJ. Analysis of microchannel heat sinks for electronics cooling. Int J Heat Mass Transf 2002;45(24):4857–69.

[34] Bazant ZP, Cedolin L. Stability of structures. Oxford: Oxford University Press; 1991.

[35] Nordstrand T, Carlsson LA, Allen HG. Transverse shear stiffness of structural core sandwich. Compos Struct 1994;27(3):317–29.

[36] Tarhini KM, Frederick GR. Wheel load distribution in I-girder highway bridges. J Struct Eng 1992;118(5):1285–94.

[37] Timoshenko S P. Strength of materials. New York: David Van Nostrand Company, Inc., 3rd Ed.; 1957.

[38] ISO 6892-1. Metallic materials-tensile testing-part 1: method of test at room temperature ISO; 2009.

[39] Su P-B, Han B, Yang M, Wei Z-H, Zhao Z-Y, Zhang Q-C, et al. Axial compressive collapse of ultralight corrugated sandwich cylindrical shells. Mater Des 2018;160:325–37.

[40] Huang Q, Choe J, Yang J, Hui Y, Xu R, Hu H. An efficient approach for post-buckling analysis of sandwich structures with elastic-plastic material behavior. Int J Eng Sci 2019;142:20–35.

[41] Romanoff J, Varsta P. Bending response of web-core sandwich plates. Compos Struct 2007;81(2):292–302.

[42] Feng S, Sun S, Yan H, Shi M, Lu TJ. Optimum composition of gas mixture in a novel chimney-based LED bulb. Int J Heat Mass Transf 2017;115:32–42.